Morphological transitions in organic submonolayer films due to variations in the surface energy of native silicon oxide substrates

Cristiano Albonetti,[1,*,†] Emilio Lorini,[2,*] Franco Dinelli,[3] Stefano Donati,[1,‡] and Luca Muccioli[2]

[1]*Consiglio Nazionale delle Ricerche—Istituto per lo Studio dei Materiali Nanostrutturati (CNR-ISMN), via P. Gobetti 101, 40129 Bologna, Italy*

[2]*Dipartimento di Chimica Industriale "Toso Montanari," University of Bologna, via P. Gobetti 85, 40129 Bologna, Italy*

[3]*Consiglio Nazionale delle Ricerche - Istituto Nazionale di Ottica (CNR-INO), via G. Moruzzi 1, 56124 Pisa, Italy*

(Received 18 May 2026; accepted 20 October 2026; published 12 November 2026)

Submonolayer-thick films of sexithiophene molecules, vapor deposited on a set of native silicon oxide substrates with variable surface energy, were investigated using atomic force microscopy. A set of morphological descriptors was employed to describe the formation of molecular islands. This formation is proven to be dependent on the surface energy and specifically linked to the doping concentration of the silicon wafers. The existence of a concentration range, for which all morphological descriptors change, suggests an interpretation of the surface energy role at the early stage of the film growth different from that introduced by Bauer for epitaxial growth. Using atomistic theoretical models, we calculated the energy values involved in the process, the number of molecules of the critical nucleus and, the step barriers faced by the molecules to ascend, or descend, from the substrate to the island. Step barriers extracted from morphological measurements match with those obtained from molecular dynamics simulations. Our findings indicate that nucleation and island formation in submonolayer films on inert substrates are correlated to the surface energy on a molecular scale.

DOI: 10.1103/h6jw-r5st

I. INTRODUCTION

Organic ultrathin films, with thickness values ranging from a few molecular layers down to a monolayer, are central to organic electronics, optoelectronics, and sensing [1]. Charge transport, optical response, and stability are all governed by their nanoscale morphology and molecular packing [2]. Among other techniques [3], organic molecular beam deposition (OMBD) [4] enables one to control the film growth at the earliest stages (nucleation, island formation, and coalescence) that are essential to determine whether the film becomes continuous, highly ordered, and ultrathin, or rough and discontinuous [5]. For instance, the morphology of an organic semiconductor film at the interface with a certain dielectric gate influences the electrical performances of an organic thin film transistor [6,7]. The accumulation layer, where the charge carriers are capacitively generated, is confined to a region immediately next to the dielectric surface and its morphology is tightly dependent on the earliest growth stages. This is particularly evident in layered organic films composed of rodlike molecules [8,9]. Studies of the film morphology have helped to localize the accumulation layer firstly in the monolayer next to the dielectric interface [7], then in the first two [10] or three [11] monolayers and, more recently, in the space region between them [12].

A key parameter connecting the film growth and the substrate is the surface energy, which controls wetting and heterogeneous nucleation barriers [8,13]. A systematic variation of the substrate surface energy, via chemical functionalization or employing different dielectric/oxide layers, can promote a higher crystallinity, improved molecular ordering, and enhanced domain alignment. It may lead also to order-of-magnitude improvements in charge carrier mobility [14–18]. These effects have been studied at the earliest stages of film growth for the case of: silicon oxide (SiO_x) [19], SiO_x compared to polymers [20], solely polymers [21,22], and functionalized silicon surfaces [16,19]. Those investigations are certainly important attempts, but the substrates employed were generally few and a complete surface energy characterization was missing or only partially done [18,21,23]. This latter point is particularly relevant for the comprehension of this phenomenon since the macroscopic surface energy is often invoked to predict the morphological evolution [13]. However, its role for the case of inert substrates [24] and at the very early growth stages is yet poorly understood.

The present work aims at improving the comprehension of these connections by combining the use of a set of native silicon oxide (n-SiO_x) substrates, fully characterized in terms of surface energy [25], with an analysis that employs a large set of descriptors [26–30] to rationalize the morphological evolution of the organic films in combination with atomistic

*These authors contributed equally to this work.

†Contact author: cristiano.albonetti@cnr.it

‡Present address: Bookmark s.r.l., Via Eugenio Bertini, 247, 47122 Forlì, Italy.

Published by the American Physical Society under the terms of the Creative Commons Attribution 4.0 International license. Further distribution of this work must maintain attribution to the author(s) and the published article's title, journal citation, and DOI.

TABLE I. Columns from left to right: wafer number, type of dopant, extrinsic semiconducting type (i.e., *n*- or *p*-type), resistivity (ρ) range measured and reported by the producers, doping concentration N, surface energy γ_S. The range of ρ considers overall changes on the whole wafer surface [33]. These ranges are converted into average doping concentration N, using an online calculator [34]. N is calculated averaging the doping concentration of the extremes of the resistivity range, while the absolute error reported is equal to half of their difference. For wafers without a precise resistivity value (No. 1), N is fixed to the converted maximum ρ value, viz. 0.0015 Ω cm, corresponding to 6.2×10^{19} cm^{-3}, whereas its absolute error is set to a relative error of 4%, as reported in the literature [35]. The table is ordered for increasing ρ and the data are taken from Ref. [25]. The absolute errors for γ_S are determined both from the variability of the contact angle values on at least three different regions and from the fitting error values obtained through the Owens-Wendt equation used to evaluate γ_S [25]. In most of the cases, such errors are consistent with the ones reported in the literature [36,37].

No.	Dopant	Type	ρ(Ω cm)	N (cm^{-3})	γ_S (dyn cm^{-1})
1	As	n	<0.0015	$>(6.2 \pm 0.3) \times 10^{19}$	27 ± 6
2	P	n	0.07–1	$(7.3 \pm 6.8) \times 10^{16}$	24 ± 6
3	B	p	0.8–1.2	$(1.6 \pm 0.3) \times 10^{16}$	18 ± 10
4	P	n	1–10	$(3 \pm 2) \times 10^{15}$	25 ± 6
5	B	p	10–12	$(1.4 \pm 0.1) \times 10^{15}$	39 ± 6
6	P	n	7	$(6.5 \pm 0.1) \times 10^{14}$	30 ± 7
7	B	p	500–1000	$(2.0 \pm 0.7) \times 10^{13}$	20 ± 7

models [31]. Since the surface energy depends on the doping concentration of Si (N), the morphological analysis has been performed as a function of N, eventually correlating the surface energy and morphological descriptors. The sole substrate effect can be isolated by fixing the total mass of the deposited molecules and carefully choosing the substrate temperature (T_S) within a given interval where no morphological transition occurs [32].

II. MATERIALS AND METHODS

A. Molecule depositions and native SiO_x substrates

A home-built OMBD system in high vacuum (HV, base pressure of 2×10^{-8} mBar), equipped with a home-built Knudsen cell (KC), was used to deposit sexithiophene molecules (6T, in powder from Sigma Aldrich) on Si substrates coated with an n-SiO_x layer. The films were deposited on ≈0.5×0.5 cm^2 pieces, cut from commercial polished Si wafers with different resistivity ρ (in Ω cm), i.e., a different doping concentration N (in cm^{-3}), obtained by incorporating a dopant (viz. B, P, or As) during the semiconductor ingot growth (see Table I). T_S was set below 353 K, above which a faster 3D growth of the film occurs [25].

Based on our recent findings [25], the surface energy (γ_S) of n-SiO_x substrates depends on both doping type and concentration N. As visible in Fig. 1, the dependence of γ_S vs log(N) is generally flat but presents a Gaussian peak centered at $\log(N_P) \approx 15.07$, viz. $N_P \approx 1.2 \times 10^{15}$ cm^{-3} (dotted purple line), with a maximum of ≈40 dyn cm^{-1} and width [14.5; 15.64], viz. $[3.2 \times 10^{14}; 4.4 \times 10^{15}]$ cm^{-3}, given by $\log(N_P) \pm 3\sigma$, where σ is the standard deviation of the

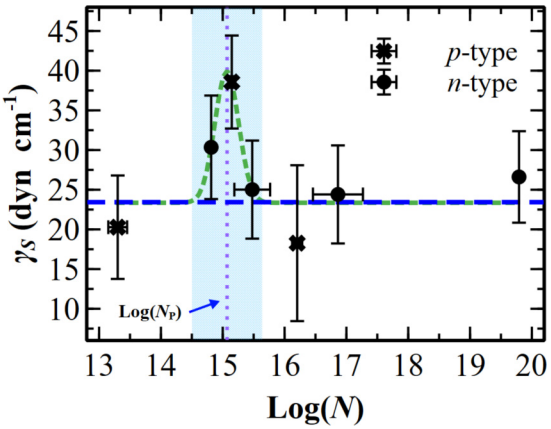


FIG. 1. Surface energy γ_S vs N. The points labeled with crosses refer to *p*-type samples, and with circles to *n*-type samples. The γ_S baseline is the dashed blue line, whereas the dashed green line shows a Gaussian peak. The semilogarithmic scale plot with a six order of magnitudes in the x axis can be transformed in a linear plot by calculating the log of the data with symmetrical error bars [38].

Gaussian distribution (light blue region). Within the experimental errors, the substrates falling out of the peak have a value of (23 ± 6) dyn cm^{-1} and define a baseline for γ_S (dashed blue line).

A quartz crystal micro-balance (QCM) placed close to the substrate was used to monitor the deposited mass m with a sensitivity of 1 ng. To eliminate any thermal drift, the QCM was kept at 293 K with a water cooler.

Pieces of all substrates were glued with silver paint on a circular sample holder with a diameter of 3 cm, fully covering the available space. However, the samples experience a different molecular flux due to the geometrical configuration of the OMBD system. With respect to an ideal KC orthogonal to the sample surface, the central samples receive 2% less of molecules, while the peripherical ones an additional 3% less [see Supplemental Material (SM) [39]]. To grow submonolayer films, i.e., films with a surface coverage $\Theta \leqslant 0.4$ ML,[1] m was calibrated by depositing 35, 47, and 60 ng on a piece of wafer No. 1 at room temperature, i.e., $T_S = 297$ K. In these experimental conditions, molecular desorption can be considered negligible [19,40] and the sticking probability of molecules $S = 1$ [41–44]. A deposition of $m = 50$ ng determines a coverage of $\Theta \approx 0.4$ ML on all the substrates. The systematic relative error due to the QCM sensitivity is 2%, hence in total the geometrical configuration of the OMBD system produces a relative error from 4 to 5%. Such relative errors replace the experimental ones when the latter are lower. All the submonolayer films were obtained by fixing the deposition rate $\mathscr{R}$ to ≈4 ng min^{-1}, while T_S was varied to investigate molecular activated processes, viz. (297 ± 1), (327 ± 2), and (349 ± 2) K (see SM [39]).

[1]A monolayer (ML) film is defined as a layer of ordered and closely packed molecules orthogonal to the surface that completely covers it: i.e., $\Theta = 1 = 100\%$. Thus, 1 ML of 6T molecules on SiO_x corresponds to a 24-Å-thick films [45–47].

B. Morphological descriptors

Topographic images were recorded with the intermittent contact mode of atomic force microscopy (AFM) and used to investigate the morphology of the submonolayer films as a function of T_S. Standard parameters, namely, island density δ (in μm^{-2}), average island area $\tilde{A}$ (in μm^2), and surface coverage Θ (in ML) were employed to describe the morphological evolution [46–48]. In addition, the interstitial space ℓ separating the islands, the fractal dimension of the islands D_f, and their average height H were also determined (see SM). All the morphological parameter values reported in the manuscript represent average values calculated on a minimum of 3 to a maximum of 5 topographic images collected in different sample areas. Since the number of analyzed islands is always $\geqslant 100$, all the parameters can be considered global, i.e., representative of the samples for any scan size [47–49] (see SM [39]).

C. Material parameters involved in the growth process

Together with $\mathscr{R}$ and T_S, Venables *et al.* [49–51] introduced three independent material parameters to describe the behavior in the early stages of nucleation and growth: reevaporation energy E_a, diffusion energy E_d, and binding energy E_i. The molecular processes responsible for the nucleation and the growth of the islands in the submonolayer regime can be seen in Fig. 1 of Refs. [50–52]. Specifically, the molecules arriving on the substrate from the KC vapor with a rate $\mathscr{R}$ are fully adsorbed if $T_S \leqslant 297$ K. Once adsorbed, they start to diffuse on the surface and stop in the most energetically favorable positions. The diffusion coefficient D depends on both T_S and E_d, the potential energy barrier to diffusion, resulting in a diffusion length $L_D = \sqrt{(D \cdot \tau)}$, i.e., the average distance covered by the molecules until they reach their final position in the mean residential time τ spent by molecules to explore the surface. For increasing T_S, reevaporation of the molecules from the surface may occur, thus reducing τ. Initially, the growth process proceeds with the formation of small populations of metastable clusters formed by j monomers, that continuously nucleate and dissolve. The number of adsorbed molecules increases during the deposition, and therefore the metastable clusters can form with an increasing number j of molecules. Once j reaches the critical value i, the so-called critical nucleus size, the clusters become stable, viz. they do not dissolve anymore. Then, the deposited molecules are captured by stable clusters becoming islands.

Starting from a substrate devoid of stable clusters, the density of critical clusters δ can be calculated using the equilibrium relationship [50–52]:

$$\delta = C \cdot e^{\left(\frac{E}{k_B T_S}\right)}, \tag{1}$$

where E is the activation energy barrier to form a stable cluster, k_B is the Boltzmann constant (in $eV\,K^{-1}$), and C is a constant depending on both the molecular diffusion and critical number i [47–49].

By definition, E is a combination of i and the three parameters E_a, E_d, and E_i [49–51]. The binding energy E_i refers to the energy gain to form a critical nucleus. The value i is attainable from the island-size distribution in the submonolayer regime

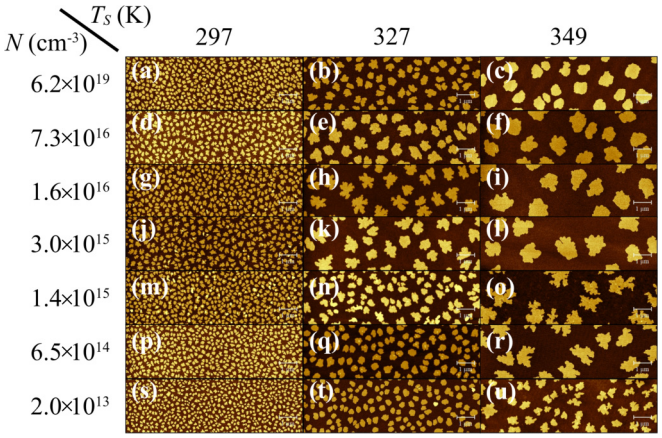


FIG. 2. Topographic images of submonolayer films obtained by depositing 50 ng of molecules for increasing T_S (left to right) and decreasing doping N (top down). The size of the images is constant and equal to $10 \times 3\,\mu m^2$. The false color z scale palette ranges from 0 (dark) to 6 nm (bright) for all images.

[26]. According to the dynamic scaling assumption [30,52–54], the island-size distribution $N_A(\Theta)$, correspondent to the density per site of islands with an area A at a coverage Θ, can be written in the general scaling form

$$\frac{N_A(\Theta) \cdot \tilde{A}^2}{\Theta} = f_i(u) \;\Rightarrow\; f_i(u) = \frac{(\Gamma[(i+2)\cdot a_i])^{(i+1)}}{a_i \cdot (\Gamma[(i+1)\cdot a_i])^{(i+2)}} \cdot u^i \cdot e^{-i a_i u^{1/a_i}}, \tag{2}$$

where $u = A/\tilde{A}$ and a_i is a constant. The normalized frequency histogram $N_A(\Theta)\cdot \sim A \cdot \Theta^{-1}$ vs $A/\tilde{A}$ can be fitted with Eq. (2) to obtain the critical nucleus size i, a natural number, from the best fitting curve yielding the highest coefficient of determination R^2 (see SM of Refs. [48,49,53–55]).

The reevaporation activation energy E_a can be evaluated by considering only the molecules desorbing from a homogeneous surface. Assuming the adsorption probability equal to the reevaporation probability, the surface coverage Θ simply follows the Langmuir equation [54–56]:

$$\frac{\Theta}{1-\Theta} \propto e^{-E_a/k_B T_S}. \tag{3}$$

Lastly, the diffusion energy E_d refers to the molecular diffusion on the substrate.

III. EXPERIMENTAL RESULTS

Figure 2 shows some topographic images of submonolayer 6T films grown on n-SiO_x for decreasing doping concentration N (top down) and increasing T_S (left to right).

The samples grown at 297 K are characterized by small islands with a high superficial density. On one hand, the islands become larger and less dense for increasing T_S [55–57]. On the other hand, less dense films form in the N range $[3 \times 10^{15}; 7.3 \times 10^{16}]\,cm^{-3}$, along with an evolution of the island shape from round to dendritic [56–58]. Since morphological variations occur where γ_S shows the Gaussian peak ($[2.5 \times 10^{14}; 4.4 \times 10^{15}]\,cm^{-3}$), the film growth might be

related to the macroscopic surface energy. Bauer theory on the epitaxy of a film [8,13] links the surface energy of the substrate γ_S, the surface energy of the molecules arriving on the surface γ_M from vacuum, and the substrate-molecule interfacial energy γ_I to $\Delta\gamma$, according to the following relationship [47–49,55–57]:

$$\Delta\gamma = \gamma_M + \gamma_I - \gamma_S. \tag{4}$$

This theory helps predict the modality of growth. If $\Delta\gamma > 0$, there is a spontaneous tendency to of the film to dewet, following the Volmer–Weber mode, whereas if $\Delta\gamma < 0$ it follows the Frank–van der Merwe one (also known as layer by layer) [8,58–60]. In the case of separated molecules deposited on an inert substrate, $\gamma_I \approx 0$ [59–61] and the energy provided to the substrate per second is $\gamma_M \approx 5 \times 10^{-6}\,\mathrm{dyn\,cm^{-1}}$. Both are negligible compared to the γ_S values of Fig. 1. Equation (4) can be thus reduced to $\Delta\gamma \approx -\gamma_S$. At low coverage values, the growth process is therefore governed solely by γ_S and the film follows the Frank-van-der-Merwe mode.

A. Standard morphological parameters

As expected from the exponential argument of Eq. (1), δ decreases for increasing T_S [see Fig. 3(a)], whereas it follows a nonmonotonic trend vs N with a minimum $\delta_{\min}$ at the characteristic concentration $\log(N_C) \approx 15.48$ (dotted blue line), off-center with respect to the center of the Gaussian peak at $\log(N_P) \approx 15.07$. As γ_S increases, δ decreases, and the surface energy acts as an increase of T_S or a decrease of $\mathscr{R}$ [60–62], in both cases correspondent to an increase of L_D [61–63]. Critical nucleus sizes instead remain roughly constant at all temperatures and for all surfaces (see SM [39]). The nonequilibrium crystal-growth framework developed by Krug and coworkers [62–65] and by Pimpinelli and Villain [65–67] was adopted to interpret the dependence of δ vs $\log(N)$. In this approach, the morphological observables are governed by diffusion-mediated nucleation processes, kinetic crossovers, and scaling relations rather than by coarsening mechanisms based on thermodynamics, such as the Gibbs-Thomson description of grain growth [66–69].

According to this interpretation, $\delta_{\min}$ can be regarded as the manifestation of a kinetic crossover associated with a characteristic doping concentration $\log(N_C)$. In this framework, the physical observables are expressed as power laws of the distance from a characteristic control parameter [69,70]. As only seven experimental points were available for each T_S, the extraction of universal scaling exponents was considered inappropriate. Based on the work of Thompson [68], the coarsening evolution of the film grains is driven by a surface energy anisotropy giving rise to cusplike behavior around a minimum. Similarly, the experimental trends can be described by using a phenomenological asymmetric crossover cusp function defining the existence of two scaling regimes induced by $\log(N)$ [71,72]:

$$\delta = \begin{cases} \delta_{\min} + A_L|\log(N) - \log(N_C)|^{o_L}, & \log(N) \leqslant \log(N_C) \\ \delta_{\min} + A_R|\log(N) - \log(N_C)|^{o_R}, & \log(N) > \log(N_C), \end{cases} \tag{5}$$

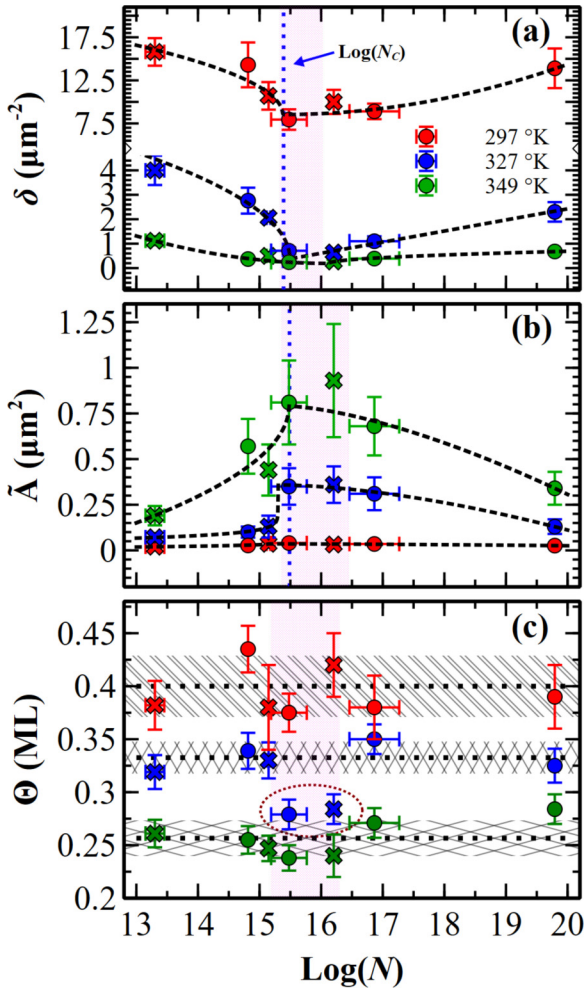


FIG. 3. Density of critical clusters δ (a), average island area $\tilde{A}$ (b), and coverage Θ (c) vs $\log(N)$ for three T_S values. The black dashed lines in (a) and (b) represent the fittings obtained with an asymmetric crossover cusp. The two exemplificative dotted blue lines mark the discontinuity position at $\log(N_C)$ for $\delta_{\min}$ (a) and $\sim A_{\max}$ (b) at 297 and 349 K, respectively. Magenta regions represent the confidence intervals of $\delta_{\min}$ and $\sim A_{\max}$ for each T_S. At 297 and 349 K, Θ can be considered constant (double inclined lines and diagonal cross regions). On the other hand, Θ can be considered constant at 327 K (vertical cross region), except for two points (dotted ellipse) defining the width of the magenta region for Θ vs $\log(N)$. The points labeled with crosses refer to *p*-type samples, with circles to *n*-type samples.

where A_L and A_R are values describing the low- and high-doping branches, respectively. The exponent pair (o_L, o_R) was systematically varied, obtaining the optimal values by minimizing the weighted reduced chi-square test. The resulting fits should not be regarded as evidence of universal critical exponents but as a compact phenomenological description of a kinetic crossover in order to evaluate a characteristic doping interval. From data fitting, $\delta_{\min}$ may be located at (15.55 ± 0.15), (15.80 ± 0.25), and (15.95 ± 0.20) for 297, 327, and 349 K, respectively. Accordingly, the kinetic crossover interval is $15.40 \lesssim \log(N_C) \lesssim 16.15$ [see light magenta region in Fig. 3(a)].

Since the deposited mass m is constant for all N and T_S values, the smaller δ is, the larger the island average area $\tilde{A}$ [60,73]. The largest islands can be obtained around $\log(N_A)$, even at 297 K where such an effect is hindered by the plot scale [see Fig. 3(b)]. The $\tilde{A}$ vs $\log(N)$ plots show opposite trends with respect to those observed for δ vs $\log(N)$. Also, the $\tilde{A}$ area exhibits a nonmonotonic dependence on $\log(N)$, with a maximum average area $\sim A_{max}$ located at (15.50 ± 0.15), (15.85 ± 0.35), and (16.20 ± 0.25) for 297, 327, and 349 K, respectively. The kinetic crossover interval is therefore stretched to $15.35 \lesssim \log(N_C) \lesssim 16.45$ [see light magenta region in Fig. 3(b)].

The surface coverage Θ was calculated by including the portions placed at the edges of the AFM images, which are not considered in the evaluation of $\tilde{A}$ and δ. With respect to other standard parameters, Θ shows a significantly weaker dependence on N than either δ or $\tilde{A}$. At 297 K, Θ remains nearly constant within the experimental uncertainty, varying between approximately 0.38 and 0.44 [see Fig. 3(c)]. At higher T_S (327 K and 349 K), a shallow but reproducible minimum develops in the interval $15.20 \lesssim \log(N_C) \lesssim 16.28$ [light magenta region in Fig. 3(c)], where the coverage decreases of about 15−20% relative to the surrounding doping levels. This interval coincides with the range in which δ reaches its minimum and $\tilde{A}$ its maximum. Since the deposited mass m of molecules is fixed, Θ may be approximated given by $\Theta \propto \delta \cdot \tilde{A}$ and, under strict mass conservation and purely lateral growth. A decrease in δ should therefore be compensated by a proportional increase in $\tilde{A}$, leading to an approximately constant coverage.

The experimental results satisfy only partially this expectation. Although δ_{min} is accompanied by a clear increase in $\tilde{A}$, the compensation is not complete, and a shallow coverage minimum remains observable at higher T_S. As all the experiments were performed in the submonolayer regime [26,74], island coalescence is negligible and thus the coverage minimum can be interpreted in terms of a modification of nucleation and growth kinetics. Indeed, looking at the data at fixed $\log(N)$, Θ decreases for increasing T_S due to both reevaporation and/or reorganization phenomena. In particular, Θ halves when passing from 297 to 349 K, hence reevaporation cannot be neglected [49].

B. Additional morphological parameters

The interstitial space ℓ separating the islands was calculated on 5×5, 10×10, and $20 \times 20\,\mu m^2$ at 297, 327, and 349 K, respectively. As shown in Fig. 4(a), ℓ follows the same trend of the average area $\tilde{A}$ [cf. Fig. 3(b)]; therefore, the larger the islands, the more spaced apart they are.

Like standard morphological parameters, the evolution of ℓ with $\log(N)$ is nonmonotonic. At 297 K, ℓ increases from approximately 85 nm at low $\log(N)$ to a maximum value ℓ_{max} of about 109 nm near $\log(N_C) \approx 15$ before decreasing again at higher $\log(N)$. The anomaly becomes considerably stronger with increasing T_S, reaching ℓ_{max} of approximately 478 nm at 327 K and 943 nm at 349 K. Despite the strong increase in magnitude, the position of ℓ_{max} remains confined within the interval $15.00 \lesssim \log(N_C) \lesssim 16.45$, in line with previous ranges [light magenta region in Fig. 4(a)]. An asymmetric-cusp analysis yields $\log(N_C)$ located at (15.48 ± 0.15), (15.15 ± 0.15), and (16.20 ± 0.25) for 297, 327, and 349 K, respectively.

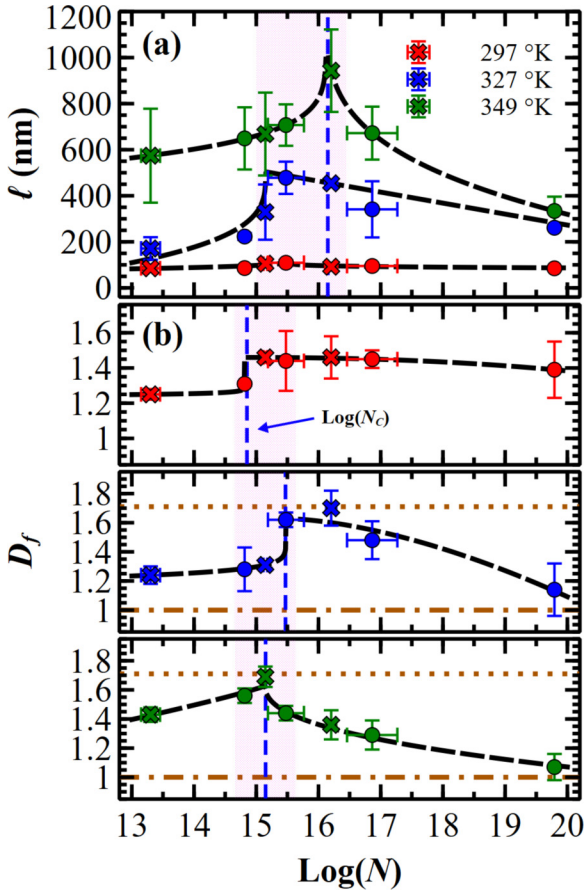


FIG. 4. Interstitial space ℓ (a) and fractal dimension D_f (b) vs $\log(N)$ for three T_S values. The data were fitted with an asymmetric crossover cusp. Magenta regions represent the confidence intervals of ℓ_{max} (a) and the maximum of D_f for each T_S. The dashed blue line indicates the critical value $\log(N_C)$. The dashed-dotted and dotted brown lines indicate the limits for the island shape (1 circular, and 1.71 fractal). The points labeled with crosses refer to p-type samples, with circles to n-type samples.

The behavior of ℓ is fully consistent with the trends observed for δ and $\tilde{A}$. An increase of ℓ occurs simultaneously with a pronounced reduction of δ and an increase in $\tilde{A}$, indicating that the islands become progressively more separated as $\log(N)$ approaches the critical interval. Within the diffusion-controlled nucleation framework proposed by Krug, this behavior can be explained with an enhancement of the adatom diffusion length. An increased adatom mobility reduces the probability of stable nucleus formation, leading to fewer islands and consequently larger empty regions between them.

Comparing Figs. 3(a) and 4(a), a higher δ correspond to a smaller ℓ; hence the molecules arriving later on the substrate are quickly captured by the neighboring islands [40].

The fractal dimension D_f is an appropriate way to quantify the island shape [47,56,75,76]. Specifically, D_f is 1 for perfectly round islands [see the dashed-dotted brown line in the middle and bottom panels of Fig. 4(b)] [77] and 2 for islands

with highly ramified contours [78], passing through randomly ramified aggregates governed by diffusion limited aggregation [$D_f = 1.71$, see the dotted brown line in the middle and bottom panels of Fig. 4(b)] [79]. Using Fig. 4 of Ref. [80] as a reference, the island shape can be termed compact ($D_f \approx 1$), dendritic ($D_f \approx 2$), or fractal ($D_f \approx 1.71$), i.e., its shape is regular (e.g., a circle) [81], has (few or many) branches characterizing preferred growth directions [76] or is highly randomly ramified [75,80], respectively.

Regardless of $\log(N)$, D_f at 297 K is always dendritic and it increases from ≈1.2 to ≈1.5 at $\log(N_C)$, and then it remains practically constant [see the magenta dashed line in Fig. 4(b), top panel]. For increasing T_S, the island shape experiences a marked evolution vs N. For 327 K, D_f evolves from dendritic to fractal for $\log(N) \rightarrow \log(N_C)^{(-)}$ and thus an increase of γ_S promotes a faster growth rate of dendrites rather than an edge diffusion [82]. For $\log(N) \rightarrow \log(N_C)^{(+)}$, the island shape evolves linearly from fractal to almost rounded at the highest $\log(N)$ [Fig. 4(b), middle panel], thus edge diffusion becomes progressively faster than the growth rate. The same trend can be observed at 349 K, but the island shape changes drastically from highly to less ramified at $\log(N_C)$ [Fig. 4(b), bottom panel]. An asymmetric-cusp analysis yields $\log(N_C)$ located at (14.81 ± 0.15), (15.48 ± 0.15), and (15.15 ± 0.15) for 297, 327, and 349 K, respectively, and the maximum of D_f is confined within the interval $14.66 \lesssim \log(N_C) \lesssim 15.63$ [light magenta regions in the three panels of Fig. 4(b)].

The height of the 6T islands was recently found to be higher than the interlayer space d measured with x-ray scattering, usually adopted as the standard island height [45,48]. The exceeding part, up to ≈1.2 nm, was ascribed to a disorder molecular layer that forms atop the 6T terraces during the deposition process.

The evolution of H vs N and T_S confirms these results [Fig. 5(a)], except for the highest doping concentration at 327 K [middle panel of Fig. 5(a)]. The height is always higher than both those one of the 6T disordered phase at low T_S with $d = 2.44$ nm (β phase [83], dotted brown lines in the middle panel of Fig. 5(a) and of the ordered phase at high T_S with $d = 2.24$ nm [γ phase [84], dashed-dotted brown lines in the middle panel of Fig. 5(a)]. At all T_S, H shows a dependence on the substrate (i.e., on γ_S) with variable crossover values. In detail, H at 297 K shows a minimum at $\log(N_C) \approx 15.5$ although H variations are small [(≈only 0.3 nm, from ≈3.2 to ≈3.5 nm—top panel of Fig. 5(a)]. For increasing T_S to 327 K, H shows a maximum of ≈4.1 nm at $\log(N_C) \approx 15.15$, i.e., where δ is minimum. Such value is substantially larger than the heights measured at both lower and higher doping concentrations, and its occurrence close to the δ minimum suggests that enhanced adatom diffusion not only suppresses nucleation but also promotes temporary vertical growth [middle panel of Fig. 5(a)]. At the highest T_S, H shows the maximum difference with respect to d equal to ≈1.5 nm, decreasing linearly from ≈4 nm to ≈2.5 nm where it forms an angular point at $\log(N_C) \approx 16.5$ with an increasing line reaching a value ≈3.1 nm [bottom panel of Fig. 5(a)]. The minimum H of ≈2.9 nm occurs in the interval $16.15 \lesssim \log(N_C) \lesssim 16.85$ where $\tilde{A}$ and ℓ are close to their maximum values, indicating that the enhanced diffusion regime at high temperature mainly promotes lateral spreading rather than vertical thickening. An asymmetric-cusp analysis yields $\log(N_C)$ located at (15.5 ± 0.2), (15.15 ± 0.10) and (16.5 ± 0.20) for 297, 327, and 349 K, respectively, and minima and maximum of H are confined within the interval $15.05 \lesssim \log(N_C) \lesssim 16.7$ [light magenta regions in the three panels of Fig. 5(a)].

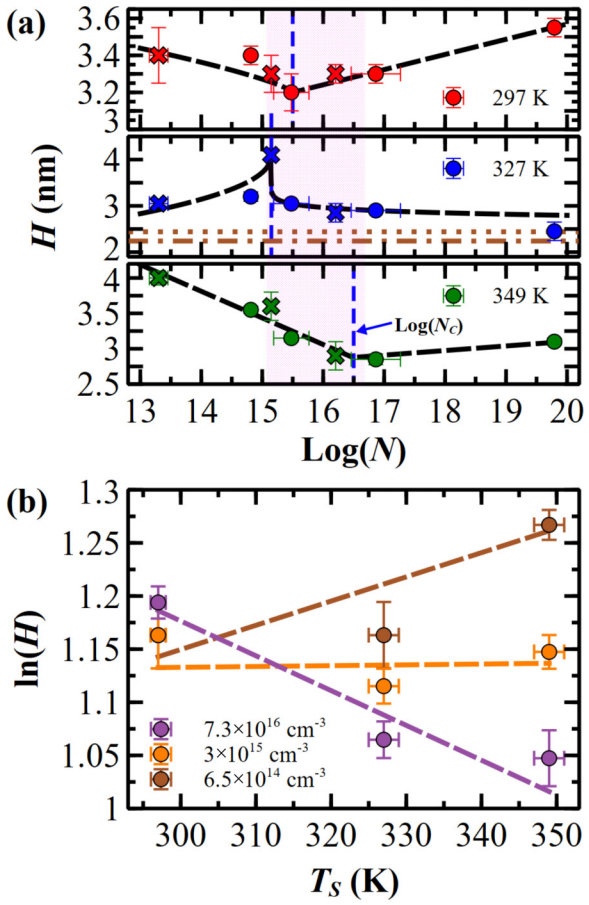


FIG. 5. (a) Island height H vs $\log(N)$: three panels, one for each T_S. (b) $\mathrm{Ln}(H)$ vs T_S: three N values are chosen to highlight different linear behaviors in semilogarithmic scale (dashed lines).

Semilogarithmic plots of H vs T_S help to understand the evolution of H vs N. As predicted in Ref. [48], H is linearly dependent on T_S in semilog scale but its slope changes with N [see Fig. 5(b)]. In particular, the slope can be positive when H increases for increasing T_S, negative or even null. These possibilities were considered in the step flow growth where an inverse step barrier (SB) effect, i.e., molecules can climb terraces, is introduced [85]. In this scenario, a negative slope of H corresponds to the SB effect acting when the molecules descend from the terraces to the substrate. At the opposite, the inverse SB effect acts when the molecules ascend from the substrate to the terraces, increasing H. A null slope suggests that the ascending and descending flows of the molecules are similar and that it exists a substrate (i.e., a γ_S value) for which the ascending and descending flow values are balanced leaving H invariant of T_S.

C. Material parameters

Equation (1) predicts an Arrhenius-like dependence of the critical clusters δ (see also SM) on the activation

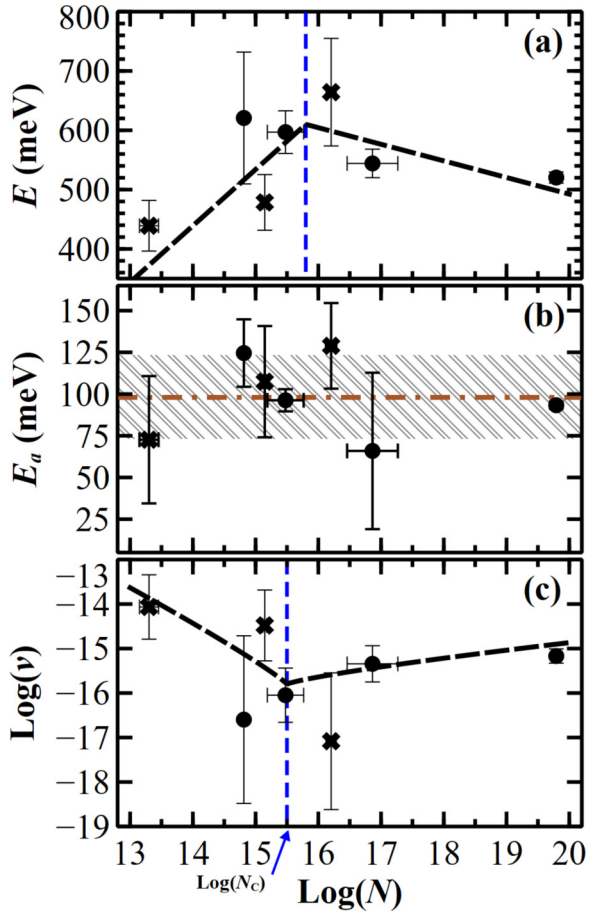


FIG. 6. Activation energy E (a), reevaporation energy E_a (b), and surface vibration frequency ν (c) vs log(N).

energy to form a stable cluster, which can be verified by plotting δ vs $(k_B T_S)^{-1}$ in a logarithmic-linear graph, which indeed follows a linear regression, yielding activation energies E ranging from ≈450 to ≈650 meV [see Fig. 6(a)]. These values clearly indicate that nucleation is more favorable on substrates with lower γ_S values (less energy required to form islands) with respect to higher ones. These values are similar to those obtained for other rodlike conjugated molecules [8,20,21,86], and they are also consistent with the energy needed to turn a 6T molecule from flat to upright [87,88]. Similarly to morphological parameters, E vs log(N) shows a maximum energy of $E = (610 \pm 40)$ meV at $\log(N_C) = (15.8 \pm 0.3)$, as obtained from the cross point of two linear fit branches of the asymmetric cusp equation [dashed black lines in Fig. 6(a)]. The $\log(N_C)$ position of the broad maximum falls inside $\log(N_C)$ intervals, where δ reaches a minimum and both $\tilde{A}$ and ℓ attain their maximum values. Although a larger activation energy would conventionally be associated with a reduced atomic mobility [89,90], the simultaneous morphological evolution indicates that the extracted quantity should be interpreted as an effective activation energy reflecting the overall kinetics of nucleation and growth. The concurrence of energetic and morphological anomalies strongly suggests that the n-SiO_x undergoes a doping-dependent modification that alters the dominant growth mechanism in the intermediate doping regime.

The same procedure can be adopted to evaluate E_a from Eq. (3). Within the experimental errors, E_a is equal to (98 ± 24) meV.[2] These signs are also consistent with the energies involved in the growth process: positive for nucleating molecules and negative for reevaporating molecules for all N values [see Fig. 6(b)].

The surface vibration frequency ν is a measure of how adsorbed molecules behave on a surface [91], tightly correlated to the mean residential time τ of a molecule on the surface [92]. Specifically, the smaller is ν the larger is τ and so the diffusion length L_D.

To exclude any additional molecular diffusion due to T_S, ν was evaluated at 297 K. As visible in Fig. 6(c), the ν plot has a minimum at $\log(N_C) = (15.5 \pm 0.3)$ falling within the $\log(N_C)$ intervals where the morphology changes and the values are similar to those reported by Venables *et al.* [49,93]. Like E, a minimum can be obtained from the cross point of two branches of an asymmetric cusp with (quasi) linear fit [dashed black lines in Fig. 6(c)]. This minimum indicates also a reduction of the effective prefactor governing molecular transport in the same doping range where the strongest morphological anomalies are observed. Based on these results, a higher γ_S corresponds to a longer L_D. Together with the maximum E, this behavior suggests a modification of the effective growth kinetics and of the oxide-mediated molecular hopping processes rather than a simple change in a single diffusion barrier.

D. Step energy barriers involved in the island height evaluation

Molecules ascending or descending topographic steps can be described as facing energetic barriers, introduced in rate equations to model the film growth [85,94–97]. In the model, the molecules participate to the film growth enlarging monolayers or developing kinks [98]. On the other hand, aggregates[3] formed either atop the terraces [48] or on the substrate [19,99–101] in submonolayer films are amorphous; they do not participate in the film growth by definition.

The contributions of amorphous aggregates to height measurements are mainly due to the layer atop the terraces, while those on the substrates are negligible (only ≈0.1 nm [48]). Accordingly, the thickness ψ of this layer can be calculated by subtracting H [Fig. 5(a)] of $d = 2.44$ nm for $T_S < 308$ K and $d = 2.24$ for $T_S > 308$ K [83], thus obtaining a value ranging from ≈0.5 to ≈1.8 nm. Considering the height of the three possible molecular orientations reported in the literature, i.e., edge-on ≈2.6 nm, side-on ≈0.6 nm, and face-on ≈0.3 nm [103], the layer atop the terraces may be composed only of side-on and face-on molecules.

Assuming that the ascending and descending flows are governed by an Arrhenius law, the thickness ψ is given by

$$\psi \propto e^{-\Delta E_{SB}/k_B T_S}, \tag{6}$$

where $\Delta E_{SB} = E_{SBdes} = E_{SBasc}$ is the difference between descending and ascending energy barriers. If $\Delta E_{SB} < 0$, ψ

[2]The activation energy E of Eq. (1) is positive as defined by Walton [51], while the reevaporation energy E_a of Eq. (3) follows an Arrhenius law, hence it is negative.

[3]With the exception of J aggregates [19,102].

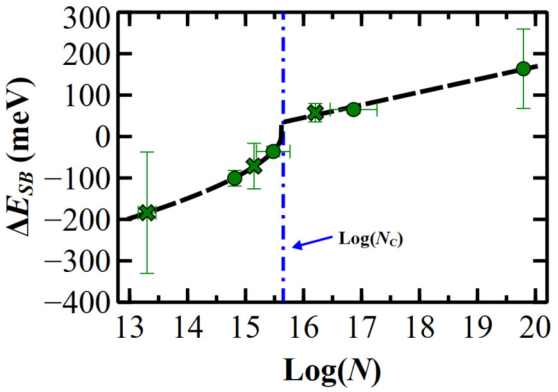


FIG. 7. Difference between descending and ascending energy barriers ΔE_{SB} vs $\log(N)$.

decreases for increasing T_S; the barrier E_{SBasc} is larger than E_{SBdes}, so that ascending a step is more difficult for a molecule. If $\Delta E_{\mathrm{SB}} > 0$, ψ increases for increasing T_S; ascending a step is energetically favored.

As shown in Fig. 7, ΔE_{SB} calculated from Eq. (6) depends on the substrate and therefore on γ_S. The cross point at $\log(N_C) = (15.65 \pm 0.15)$ falls within the $\log(N_C)$ intervals where the morphology changes. It can be obtained from the cross point of two branches of an asymmetric cusp fit (dashed black lines in Fig. 7). Notably, it exists a $\log(N)$ value for which $\Delta E_{\mathrm{SB}} \approx 0$, where the barriers are equal. Indeed, ΔE_{SB} is negative on the left of this point and ψ decreases for increasing T_S while, on the right, ΔE_{SB} is positive and ψ increases for increasing T_S. The negative left branch changes with respect to the positive one, and hence it is more sensitive to surface energy variations.

E. Molecular dynamics simulations of step energy barriers

The results presented above are compared in the following to molecular dynamics simulations for which methods are described in the SM. A n-SiO_x substrate with increasing γ_S was produced starting from a silica slab with a fixed concentration of superficial Si and O dangling atoms ($\approx 1\,\mathrm{nm}^{-2}$ to both), with a classical model which describes the interaction with 6T atoms through partial charges q and Lennard-Jones well depths ε (see Table S2 in the SM) [104]. By reducing systematically q and ε for Si and O atoms, five different surfaces were produced: (q, ε), $(q \div 2, \varepsilon)$, $(q, \varepsilon \div 2)$, $(q \div 2, \varepsilon \div 2)$, and $(q \div 3, \varepsilon \div 3)$. Their surface energy γ_S was evaluated by from droplet equilibrium simulations [105], measuring the contact angle Ξ of three solvents with decreasing liquid energy γ_L (i.e., water, glycerol, and formamide [25]). Simulations returned five surfaces with γ_S systematically decreasing moving from (q, ε) to $(q \div 3, \varepsilon \div 3)$ (see Fig. S3 and Sec. S5.2 for details). To finish the sample preparation, a 6T island was placed over each substrate [see Fig. 8(a)].

The energetic changes induced by the different surfaces were measured as the free energy E_{Pr} of a molecular 6T probe that diffuses on the surface; the larger is E_{Pr} the weaker is the interaction with the T6 island or the silica substrate. Figure 8(b) shows E_{Pr} maps for (q, ε), $(q, \varepsilon \div 2)$, and $(q \div 3, \varepsilon \div 3)$ surfaces with the average energy of the island

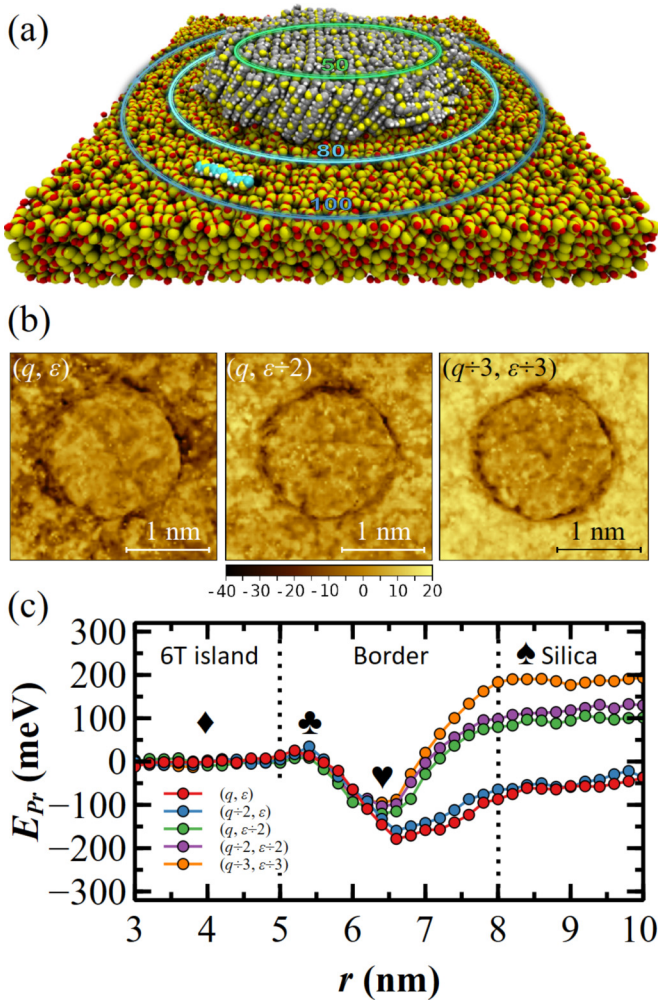


FIG. 8. (a) Perspective view of the equilibrated 6T island on the surface (q, ε), highlighting the position of the molecular probe and the circular regions with increasing radius (in Å) used for the analysis. The island region is within a radius of 50 Å, the border region range from 50 to 80 Å, and the silica surface is from 80 to 100 Å. (b) Free-energy maps of the molecular probe diffusing across the island, step-edge, and silica surface on (q, ε), $(q, \varepsilon \div 2)$, and $(q \div 3, \varepsilon \div 3)$ surfaces as calculated by using the adaptive biasing force method [106,107]. (c) Free-energy radial profiles for each surface. The initial part in the island center, $0 \leqslant r \leqslant 30$, is excluded because it is noisy as only few points were used for averaging.

terrace fixed to zero in all maps to highlight three different free-energy landscapes for the substrate/molecule interaction. Minima of the E_{Pr} maps [dark areas in the three maps of Fig. 8(b)] are located near the island/surface interface that is the most favorable region for molecular adsorption and from which the island size increases and/or its shape changes (cf. fractal dimension).

The E_{Pr} maps show also an evolution of the silica contrast from few brighter patches for a (q, ε) surface to a homogeneous contrast for a $(q \div 3, \varepsilon \div 3)$ surface. On the surface (q, ε) where q and ε are maximum (i.e., a higher γ_S), the probe adsorption is favored on silica than atop the island, while the opposite becomes increasingly preferred if q and ε are progressively weakened (i.e., lowering γ_S).

TABLE II. Free-energy barriers (meV) associated with the diffusion of a 6T molecule for each silica surface model. Reported values include the descending barrier (island to edge, E_{SBdes}), ascending barrier (edge to island, E_{SBasc}), detachment barrier (edge to silica, E_{SBsep}), and the free-energy difference between the island and silica plateaus (ΔE_{SB}).

	$(q,\ \varepsilon)$	$(q \div 2,\ \varepsilon)$	$(q,\ \varepsilon \div 2)$	$(q \div 2,\ \varepsilon \div 2)$	$(q \div 3,\ \varepsilon \div 3)$
E_{SBdes} (meV)	78	48	52	48	78
E_{SBasc} (meV)	204	195	130	113	113
E_{SBsep} (meV)	143	121	221	230	291
ΔE_{SB} (meV)	48	48	−104	−126	−191

The trend observed in the maps was quantitatively evaluated by averaging radial free-energy profiles in annular rings of 2 Å width, collected for all the surfaces [Fig. 8(c)]. Pairs of energy profiles with the same Lennard-Jones parameters are similar, viz. $(q,\ \varepsilon)$, $(q \div 2,\ \varepsilon)$, and $(q,\ \varepsilon \div 2)$, $(q \div 2,\ \varepsilon \div 2)$, suggesting that this interaction is dominant in the probe energetics (cf. Table S2 in SM), differently from the water contact angle simulations where both q and ε contribute.

Along with its diffusion, the molecular probe meets three free-energy barriers extracted from E_{Pr} radial profiles: (a) the energy rise from the plateau on the island top and the maximum at the island edge [diamonds and clubs symbols in Fig. 8(c), respectively], namely, the energy to descend the island E_{SBdes}; (b) the energy step from the minimum of the border region to the top of the edge [hearts and clubs symbols in Fig. 8(c), respectively], namely, the energy to ascend the island E_{SBasc}; and (c) the free-energy difference from the minimum of the border region and the silica surface (hearts and spades symbols in Fig. 8(c), respectively), namely, the energy cost for separating the molecular probe from the island E_{SBsep}.

From the results reported in Table II, some correlations with γ_S emerge: E_{SBasc} decreases for decreasing γ_S whereas the opposite occurs for E_{SBsep}. The descending barrier E_{SBdes} instead is poorly affected by γ_S with an average value of (61 ± 15) meV, in agreement with the Ehrlich-Schwoebel barrier for organic molecules deposited on an amorphous substrate [107–109], but it is lower compared to the ones observed on crystalline substrates, where the substrate/molecule interaction is stronger [110,111]. The energy difference between substrate and island ΔE_{SB} is notably in agreement with the experimental results: it passes from positive (lower values) to negative (larger values) and thus it may exist a silica surface model, i.e., a combination of q and ε values, for which $\Delta E_{SB} = 0$. The values calculated from the simulations are comparable with the experimental ones, validating the assumption at the basis of Eq. (6).

IV. DISCUSSION

The $\log(N_C)$ intervals resulting from an analysis of morphological and material parameters [see Fig. 9(a)] generate the final interval I, $14.66 \lesssim \log(N_C) \lesssim 16.70$ [yellow area in Fig. 9(b)]. The γ_S plot of Fig. 1 was enriched by including the full set of n-SiO_x substrates reported in Ref. [25] [three additional red crosses in Fig. 9(b)]. The interval I, where the morphological and material properties change, overlaps almost completely with the interval of the full set of n-SiO_x substrates where the surface energy γ_S changes, except for the initial part [cyan region in Fig. 9(b)].

Above $\log(N_C) \approx 15.9$, γ_S is constant within the experimental errors [right limit of the green region in Fig. 9(b)] and, accordingly, morphological and material properties should be independent of it and solely dependent on T_S. However, all morphological and materials properties change vs $\log(N)$ for all T_S [D_f, only partially see Fig. 9(a)], and thus the dependence of them vs $\log(N)$ is preserved even if hindered by the large experimental errors of the surface energy.

Within the region where γ_S increases for $\log(N) \rightarrow \log(N_P)^{(-)}$, the polar component γ_S^p of the surface increases as well [25]. On the basis of the works by Ribic *et al.* [21] and Yang *et al.* [18], γ_S^p is the main responsible for the morphological changes because the dispersive component γ_S^d measured

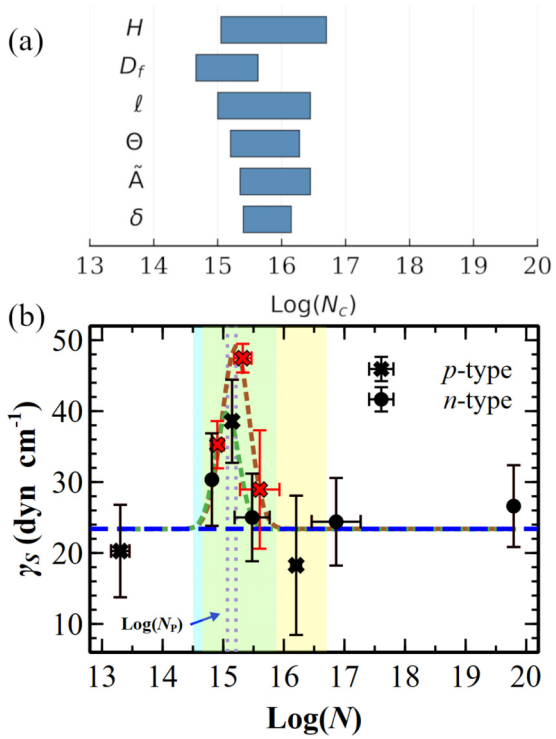


FIG. 9. (a) Graphic representation of $\log(N_C)$ intervals resulting from the analysis of the morphological and material properties (indicated as symbol). (b) Plot including the set of substrates used for this work [14.5; 15.64] and the set of data from Ref. [25] [14.535; 15.885] (light blue region) overlapped to the total interval I determined in this work (yellow region). The light green area is produced by overlapping the colors used. The two dotted lines refer to peaks centers N_P of the reduced surface energy interval adopted in this manuscript and the full interval reported in Ref. [25].

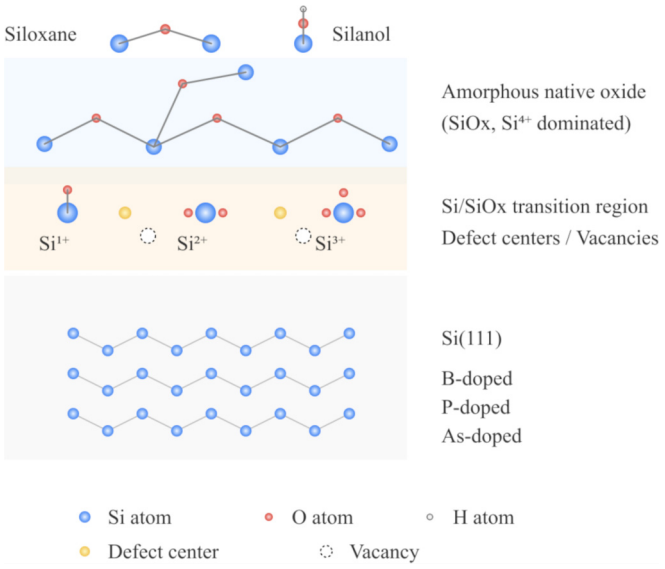


FIG. 10. Schematic representation of the proposed structure of n-SiO_x. The native oxide is described as a chemically graded layer consisting of an amorphous SiO_x region dominated by Si^{4+} species and a suboxide-rich Si/SiO_x transition region containing intermediate oxidation states (Si^{1+}, Si^{2+}, and Si^{3+}), vacancies, and defect centers (dashed circles and yellow circles, respectively). Surface silanol and siloxane groups are depicted as terminal species bonded to fully oxidized Si^{4+} centers within the amorphous SiO_x network, which gradually transitions through suboxide states toward a fully crystalline Si(111) substrate. Dopant-dependent modifications of defect populations and charge states within the transition region are proposed to influence oxide charge distribution, surface hydroxylation (silanol/siloxane balance), and, ultimately, surface energy.

in these works is constant within the experimental errors. Moreover, the higher γ_S is, the higher the sticking coefficient S (Eq. (7) in Ref. [112]), since the attractive forces between the surface and the incoming molecules increase. This is in agreement with the empiric rule for which the higher γ_S is, the higher the number of bonds with the surface [113]. The molecules deposited on the surface tend to stick at (or close) their arrival position, reducing *de facto* their L_D, and thus promoting a higher δ.

Our work, together with those by Ribic *et al.* and Yang *et al.*, propends for the opposite: the higher is γ_S is, the lower δ is [Fig. 3(a)]. Such a behavior cannot be simply ascribed to changes in roughness [114] since the surface roughness of the n-SiO_x samples in the region where γ_S changes is always $\approx$2 or $\approx$3 Å [25]. These results may be coherent only if the surface-active species are considered in the kinetic of growth, which either facilitates or inhibits the surface diffusion producing a lower or higher δ for constant T_S, respectively [115].

Such a scenario is conciliable with the experimental results obtained for n-SiO_x only if a mechanism connecting the Si doping to the surface chemical properties exists. Based on the literature, n-SiO_x can be regarded as a chemically graded layer rather than a sharp Si/SiO_2 interface (see Fig. 10). Early optical and electron spectroscopic studies suggested that n-SiO_x contains a significant fraction of partially oxidized silicon species, with a composition closer to SiO_x ($1 < x < 2$) than to stoichiometric SiO_2, supporting the existence of a transition region between a fully crystalline silicon and a fully oxidized surface layer (see Si/SiO_x transition region in Fig. 10) [116,117].

n-SiO_x is known to require the simultaneous presence of oxygen and water, with subsequent hydroxylation reactions leading to the formation of surface silanol groups and, through condensation, siloxane bridges [118]. In this framework, the dependence of the n-SiO_x properties on doping can be rationalized with defect-mediated oxidation mechanisms [119–121]. Previous studies showed that the n-SiO_x growth is influenced by dopant concentration and vacancy populations near the silicon surface [122], while a theoretical work demonstrated that silicon vacancies can exist in multiple charge states whose stability depends on the Fermi level [123]. It is also noteworthy that the diffusion mechanisms of the investigated dopants differ substantially: boron diffusion in silicon is predominantly mediated by self-interstitials, whereas phosphorus and arsenic diffusion are more closely associated with vacancy-assisted transport and dopant-vacancy complexes [124–127].

Consequently, the vacancy and trap populations proposed to influence the n-SiO_x structure cannot be explained solely by the diffusion mechanism of boron itself, but they are more likely related to changes in defect thermodynamics and charge-state equilibria induced by dopant-dependent shifts of the Fermi level [121,123]. Accordingly, changes in doping level modify the concentration and charge state of vacancy-related defects within the Si/SiO_x transition region, thereby affecting oxygen incorporation, the formation of intermediate oxidation states, and the charge distribution within the oxide. The resulting modification of the oxide electrostatic environment propagates toward the surface, altering the stability of hydroxylated sites and thus affecting the relative abundance of silanol and siloxane groups on the surface. Since silanols and siloxanes are the principal surface species governing the hydrophilic or hydrophobic character of n-SiO_x, changes in their relative concentration ultimately modify the surface energy, providing a direct link between bulk doping, interfacial defect chemistry, oxide structure, and the wettability properties observed experimentally [25].

On the basis of the mechanism described above, the density of $-$OH groups on the n-SiO_x substrates increases vs $\log(N)$ for $\log(N) \rightarrow \log(N_P{}^{(-)})$ [25], as well as γ_S, facilitating the surface diffusion with an increase of L_D and thus a reduction of δ. This is consistent with the results obtained in Fig. 6(c). This scenario also explains the apparent contradiction of a reduced i for the highest γ_S (Table S1), corresponding to a maximum of E. Indeed, a smaller critical cluster size should be correlated with a lower E [128], but the surface-active species introduce an additional energy ΔE that increases E [115], which is not included in the general Eq. (1). Finally, this interpretation corrects the empirical evidence that an increased γ_S reduces the sticking coefficient S, preventing any island nucleation [39,129–153]. A lower δ also corresponds to a larger $\tilde{A}$ and ℓ, as already mentioned in the text.

V. CONCLUSIONS

The morphology of submonolayer 6T films on native silicon oxide substrates was investigated as a function of the

substrate surface energy, obtained varying the doping concentration in the silicon wafers used. To the best of our knowledge, this is the first case of a study with a systematic change of the surface energy applied to the growth of organic materials on amorphous substrates.

The experimental data reveal that there is an interval of doping concentrations for which the surface energy changes drastically and all the morphological parameters present peculiar trends. Notably, such an interval is not centered at the maximum of the surface energy but clearly defines a region that produces a morphological transition. Similar trends can be observed for the energies involved in the kinetic growth process as well as on the step barriers that molecules encounter during the growth process. Step barriers for ascending and descending molecules were experimentally evaluated matching the results obtained from molecular dynamic simulations. This individuates a concentration value for which the energy balance can be null. Some contradictory results obtained both herein, and in the literature, can be explained if one introduces a contribution of the contaminants in the kinetic of growth, improving the understanding of the phenomena involved in the submonolayer growth. The surface energy measurements reported herein need to be improved with more precise and accurate contact angle measurements and theoretical models. In fact, the experimental errors may conceal surface phenomena that are, however, observable thanks from changes in morphological and materials properties.

ACKNOWLEDGMENTS

C.A. thanks R. Nipoti for providing substrates and Professor F. Biscarini for inspiring him to perform growth studies, especially on energy barriers measurements. AFM images were elaborated upon with the software GWYDDION [154], data were analyzed by the GNU General Public Licensed Software QTIPLOT, and figures were prepared with the GNU General Public Licensed software VEUSZ. AFM were collected in the SPM@ISMN facility. The work was supported in equal terms by the following projects: EC FP7 ONE-P large-scale Project No. 212311, EU-STREP ForceTool (NMP4-CT-2004-STRP 013684), and the National Recovery and Resilience Plan (PNRR), Mission 4, Component 2, Investment 1.1 (PRIN 2022) by the Italian Ministry of University and Research (MUR), funded by the European Union—NextGeneration EU (Grant No. 2022FWZCHK FUTURO CUP D53D23009110006).

DATA AVAILABILITY

There are no publicly available research data or software supporting this manuscript. Requests for further information or data should be sent to the authors.

[1] M. Bouachrine and S. Ayachi, Organic electronics: Pioneering the future of sustainable and flexible technology, RSC Adv. **15**, 45177 (2025).

[2] S. R. Forrest, Ultrathin organic films grown by organic molecular beam deposition and related techniques, Chem. Rev. **97**, 1793 (1997).

[3] R. D. Gould, S. Kasap, and A. K. Ray, Thin Films, in *Springer Handbook of Electronic and Photonic Materials*, edited by S. Kasap, and P. Capper (Springer International Publishing, Cham, 2017), p. 1.

[4] A. Koma, Molecular beam epitaxial growth of organic thin films, Prog. Cryst. Growth Charact. Mater. **30**, 129 (1995).

[5] H. Sitter, R. Resel, G. Koller, M. G. Ramsey, A. Andreev, and C. Teichert, Fundamentals of organic film growth and characterisation, in *Organic Nanostructures for Next Generation Devices*, edited by K. Al-Shamery, H.-G. Rubahn, and H. Sitter (Springer, Berlin, 2008), pp. 3–19.

[6] G. Horowitz, R. Hajlaoui, H. Bouchriha, R. Bourguiga, and M. Hajlaoui, The concept of "threshold voltage" in organic field-effect transistors, Adv. Mater. **10**, 923 (1998).

[7] A. Dodabalapur, L. Torsi, and H. E. Katz, Organic transistors: Two-dimensional transport and improved electrical characteristics, Science **268**, 270 (1995).

[8] G. Hlawacek and C. Teichert, Nucleation and growth of thin films of rod-like conjugated molecules, J. Phys.: Condens. Matter **25**, 143202 (2013).

[9] R. Ruiz *et al.*, Pentacene thin film growth, Chem. Mater. **16**, 4497 (2004).

[10] F. Dinelli, M. Murgia, P. Levy, M. Cavallini, F. Biscarini, and D. M. de Leeuw, Spatially correlated charge transport in organic thin film transistors, Phys. Rev. Lett. **92**, 116802 (2004).

[11] A. Shehu, S. D. Quiroga, P. D'Angelo, C. Albonetti, F. Borgatti, M. Murgia, A. Scorzoni, P. Stoliar, and F. Biscarini, Layered distribution of charge carriers in organic thin film transistors, Phys. Rev. Lett. **104**, 246602 (2010).

[12] C. Albonetti, G. Olivieri, A. Shehu, S. D. Quiroga, M. Murgia, and F. Biscarini, Unravelling molecular disorder at SAM-functionalized charge injection interfaces in organic field-effect transistors, Org. Electron. **100**, 106360 (2022).

[13] E. Bauer, Phänomenologische Theorie der Kristallabscheidung an Oberflächen. II, Z. Kristallogr. **110**, 395 (1958).

[14] B. King, C. L. Radford, M. C. Vebber, B. Ronnasi, and B. H. Lessard, Not just surface energy: The role of Bis(pentafluorophenoxy) silicon phthalocyanine axial functionalization and molecular orientation on organic thin-film transistor performance, ACS Appl. Mater. Interfaces **15**, 14937 (2023).

[15] F. Zhang, E. Mohammadi, X. Luo, J. Strzalka, J. Mei, and Y. Diao, Critical role of surface energy in guiding crystallization of solution-coated conjugated polymer thin films, Langmuir **34**, 1109 (2018).

[16] R. Ruiz, B. Nickel, N. Koch, L. C. Feldman, R. F. Haglund, A. Kahn, and G. Scoles, Pentacene ultrathin film formation on reduced and oxidized Si surfaces, Phys. Rev. B **67**, 125406 (2003).

[17] M. Sarcletti, T. Schmaltz, and M. Halik, The mutual influence of surface energy and substrate temperature on the saturation mobility in organic semiconductors, Org. Electron. **15**, 3082 (2014).

[18] S. Y. Yang, K. Shin, and C. E. Park, The effect of gate-dielectric surface energy on pentacene morphology and organic field-effect transistor characteristics, Adv. Funct. Mater. **15**, 1806 (2005).

[19] F. Dinelli, J. - F. Moulin, M. A. Loi, E. Da Como, M. Massi, M. Murgia, M. Muccini, F. Biscarini, J. Wie, and P. Kingshott, Effects of surface chemical composition on the early growth stages of α-sexithienyl films on silicon oxide substrates, J. Phys. Chem. B **110**, 258 (2006).

[20] S. Pratontep, F. Nüesch, L. Zuppiroli, and M. Brinkmann, Comparison between nucleation of pentacene monolayer islands on polymeric and inorganic substrates, Phys. Rev. B **72**, 085211 (2005).

[21] P. R. Ribič, V. Kalihari, C. D. Frisbie, and G. Bratina, Growth of ultrathin pentacene films on polymeric substrates, Phys. Rev. B **80**, 115307 (2009).

[22] N. G. Martinelli, M. Savini, L. Muccioli, Y. Olivier, F. Castet, C. Zannoni, D. Beljonne, and J. Cornil, Modeling polymer dielectric/pentacene interfaces: On the role of electrostatic energy disorder on charge carrier mobility, Adv. Funct. Mater. **19**, 3254 (2009).

[23] W. J. Huang, B. Q. Li, and J. M. Zuo, Diffusion-limited submonolayer pentacene thin film growth on hydrogen-passivated Si(1 1 1) substrates, Surf. Sci. **595**, 157 (2005).

[24] S. Verlaak, S. Steudel, P. Heremans, P. Heremans, D. Janssen, and M. S. Deleuze, Nucleation of organic semiconductors on inert substrates, Phys. Rev. B **68**, 195409 (2003).

[25] M. Della Ciana, A. Kovtun, C. Summonte, A. Candini, D. Cavalcoli, D. Gentili, R. Nipoti, and C. Albonetti, Native silicon oxide properties determined by doping, Langmuir **39**, 12430 (2023).

[26] J. G. Amar and F. Family, Critical cluster size: Island morphology and size distribution in submonolayer epitaxial growth, Phys. Rev. Lett. **74**, 2066 (1995).

[27] J. Amar, Kinetics of submonolayer epitaxial growth, Comput. Phys. Commun. **146**, 1 (2002).

[28] J. G. Amar, F. Family, and P.-M. Lam, Dynamic scaling of the island-size distribution and percolation in a model of submonolayer molecular-beam epitaxy, Phys. Rev. B **50**, 8781 (1994).

[29] A. C. Mayer, R. Ruiz, R. L. Headrick, A. Kazimirov, and G. G. Malliaras, Early stages of pentacene film growth on silicon oxide, Org. Electron. **5**, 257 (2004).

[30] R. Ruiz, B. Nickel, N. Koch, L. C. Feldman, R. F. Haglund, A. Kahn, F. Family, and G. Scoles, Dynamic scaling, island size distribution, and morphology in the aggregation regime of submonolayer pentacene films, Phys. Rev. Lett. **91**, 136102 (2003).

[31] J. A. Venables, *Introduction to Surface and Thin Film Processes* (Cambridge University Press, Cambridge, 2000).

[32] S. Chiodini, A. Straub, S. Donati, C. Albonetti, F. Borgatti, P. Stoliar, M. Murgia, and F. Biscarini, Morphological transitions in organic ultrathin film growth imaged by in situ step-by-step atomic force microscopy, J. Phys. Chem. C **124**, 14030 (2020).

[33] Freiberg instruments, resistance measurements on wafers and bricks, https://www.freiberginstruments.com/upcdmdp/applications/resistance-measurements-on-wafers-and-bricks.html.

[34] ECEn IMMERSE web team, resistivity & mobility calculator, https://cleanroom.byu.edu/ResistivityCal.

[35] J. R. Ehrstein and C. M. Croarkin, Standard reference materials: The certification of 100 mm diameter silicon resistivity SRMs 2541 through 2547 using dual-configuration four-point probe measurements, NIST Special Publication (USA) **260**, 106 (1999).

[36] A. Burdzik, M. Stähler, M. Carmo, and D. Stolten, Impact of reference values used for surface free energy determination: An uncertainty analysis, Int. J. Adhes. Adhes. **82**, 1 (2018).

[37] A. Rudawska and E. Jacniacka, Analysis for determining surface free energy uncertainty by the Owen–Wendt method, Int. J. Adhes. Adhes. **29**, 451 (2009).

[38] LeFitz, The error of the natural logarithm, https://physics.stackexchange.com/questions/95254/the-error-of-the-natural-logarithm.

[39] See Supplemental Material http://link.aps.org/supplemental/10.1103/h6jw-r5st for (1) Molecular flux from ideal and real Knudsen cells, (2) Calibration of the substrate temperature, (3) Calculation of morphological descriptors, (4) Local and global island density, (5) Critical nucleus size, (6) Regimes of molecular condensation, (7) Molecular dynamics simulations, which includes Refs. [39,130–152].

[40] S. Pratontep, M. Brinkmann, F. Nüesch, and L. Zuppiroli, Correlated growth in ultrathin pentacene films on silicon oxide: Effect of deposition rate, Phys. Rev. B **69**, 165201 (2004).

[41] B. Scherwitzl, R. Resel, and A. Winkler, Film growth, adsorption and desorption kinetics of indigo on SiO_2, J. Chem. Phys. **140**, 184705 (2014).

[42] P. Frank, T. Djuric, M. Koini, I. Salzmann, R. Rieger, K. Müllen, R. Resel, N. Koch, and A. Winkler, Layer growth, thermal stability, and desorption behavior of Hexaazatriphenylene-hexacarbonitrile on Ag(111), J. Phys. Chem. C **114**, 6650 (2010).

[43] S. Müllegger, O. Stranik, E. Zojer, and A. Winkler, Adsorption, initial growth and desorption kinetics of *p*-quaterphenyl on polycrystalline gold surfaces, Appl. Surf. Sci. **221**, 184 (2004).

[44] R. Lassnig, B. Striedinger, M. Hollerer, A. Fian, B. Stadlober, and A. Winkler, *In situ* preparation, electrical and surface analytical characterization of pentacene thin film transistors, J. Appl. Phys. **116**, 114508 (2014).

[45] J.-F. F. Moulin, F. Dinelli, M. Massi, C. Albonetti, R. Kshirsagar, and F. Biscarini, *In situ* x-ray synchrotron study of organic semiconductor ultra-thin films growth, Nucl. Instrum. Methods Phys. Res. B **246**, 122 (2006).

[46] F. Family, Scaling, percolation and coarsening in epitaxial thin film growth, Physica A **266**, 173 (1999).

[47] F. Valle, M. Brucale, S. Chiodini, E. Bystrenova, and C. Albonetti, Nanoscale morphological analysis of soft matter aggregates with fractal dimension ranging from 1 to 3, Micron **100**, 60 (2017).

[48] S. Chiodini, F. Dinelli, N. F. Martinez, S. Donati, and C. Albonetti, Identification of ultra-thin molecular layers atop monolayer terraces in submonolayer organic films with scanning probe microscopy, Ultramicroscopy **240**, 113598 (2022).

[49] J. A. Venables, G. D. T. Spiller, and M. Hanbucken, Nucleation and growth of thin films, Rep. Prog. Phys. **47**, 399 (1984).

[50] J. A. Venables, Rate equation approaches to thin film nucleation kinetics, Philos. Mag. **27**, 697 (1973).

[51] D. Walton, Nucleation of vapor deposits, J. Chem. Phys. **37**, 2182 (1962).

[52] T. Vicsek and F. Family, Dynamic scaling for aggregation of clusters, Phys. Rev. Lett. **52**, 1669 (1984).

[53] S. Lorbek, G. Hlawacek, and C. Teichert, Determination of critical island size in para-sexiphenyl islands on SiO_2 using capture-zone scaling, Eur. Phys. J. Appl. Phys. **55**, 23902 (2011).

[54] T. Dutta, N. Lebovka, and S. Tarafdar, Condensation and evaporation of mutually repelling particles: Steady states and limit cycles, Phys. Rev. E **70**, 61609 (2004).

[55] I. Markov, The influence of surface diffusion processes on the kinetics of heterogeneous nucleation, Thin. Solid. Films **8**, 281 (1971).

[56] S. Chiodini, P. Stoliar, P. F. Garrido, and C. Albonetti, Differential entropy: An appropriate analysis to interpret the shape complexity of self-similar organic islands, Materials **14**, 6529 (2021).

[57] P. Müller and R. Kern, The physical origin of the two-dimensional towards three-dimensional coherent epitaxial Stranski-Krastanov transition, Appl. Surf. Sci. **102**, 6 (1996).

[58] F. Schreiber, Organic molecular beam deposition: Growth studies beyond the first monolayer, Phys. Stat. Sol. (A) **201**, 1037 (2004).

[59] K. G. Pepper, C. Bahrim, and R. Tadmor, Interfacial tension and spreading coefficient of thin films: Review and future directions, J. Adhes. Sci. Technol. **25**, 1379 (2011).

[60] S. Pratontep, M. Brinkmann, F. Nüesch, and L. Zuppiroli, Nucleation and growth of ultrathin pentacene films on silicon dioxide: Effect of deposition rate and substrate temperature, Synth. Met. **146**, 387 (2004).

[61] A. Winkler, On the nucleation and initial film growth of rod-like organic molecules, Surf. Sci. **652**, 367 (2016).

[62] J. Krug, Origins of scale invariance in growth processes, Adv. Phys. **46**, 139 (1997).

[63] J. Krug, Statistical physics of growth processes, in *Scale Invariance, Interfaces, and Non-Equilibrium Dynamics*, edited by A. McKane, M. Droz, J. Vannimenus, and D. Wolf (Springer US, Boston, MA, 1995), pp. 1–61.

[64] J. Krug and H. Spohn, Kinetic roughening of growing surfaces, in *Solids Far from Equilibrium* (Cambridge University Press, Cambridge, 1991).

[65] A. Pimpinelli and J. Villain, *Physics of Crystal Growth* (Cambridge University Press, Cambridge, 1998).

[66] C. V. Thompson, J. Floro, and H. I. Smith, Epitaxial grain growth in thin metal films, J. Appl. Phys. **67**, 4099 (1990).

[67] C. V. Thompson, Coarsening of particles on a planar substrate: Interface energy anisotropy and application to grain growth in thin films, Acta Metall. **36**, 2929 (1988).

[68] C. V. Thompson, Secondary grain growth in thin films of semiconductors: Theoretical aspects, J. Appl. Phys. **58**, 763 (1985).

[69] T. J. Oliveira and F. D. A. Aarão Reis, Crossover in the scaling of island size and capture zone distributions, Phys. Rev. B **86**, 115402 (2012).

[70] A. Pimpinelli and P. Peyla, Crossover scaling in thick film growth on vicinal surfaces, Int. J. Mod. Phys. B **11**, 3647 (1997).

[71] X. Tian and H. Xia, Crossover effects and dynamic scaling properties from Eden growth to diffusion-limited aggregation, Phys. Lett. A **508**, 129494 (2024).

[72] W. Dieterich, M. Einax, and P. Maass, Stochastic theories and scaling relations for early-stagesurface growth, Eur. Phys. J. Spec. Top. **161**, 151 (2008).

[73] B. Stadlober, U. Haas, H. Maresch, and A. Haase, Growth model of pentacene on inorganic and organic dielectrics based on scaling and rate-equation theory, Phys. Rev. B **74**, 165302 (2006).

[74] J. G. Amar and F. Family, Kinetics of submonolayer and multilayer epitaxial growth, Thin. Solid. Films **272**, 208 (1996).

[75] R. Q. Hwang, J. Schröder, C. Günther, and R. J. Behm, Fractal growth of two-dimensional islands: Au on Ru(0001), Phys. Rev. Lett. **67**, 3279 (1991).

[76] G. S. Bales and D. C. Chrzan, Transition from compact to fractal islands during submonolayer epitaxial growth, Phys. Rev. Lett. **74**, 4879 (1995).

[77] D. Bérubé and M. Jébrak, High precision boundary fractal analysis for shape characterization, Comput. Geosci. **25**, 1059 (1999).

[78] D. Bensimon, E. Domany, and A. Aharony, Crossover of fractal dimension in diffusion-limited aggregates, Phys. Rev. Lett. **51**, 1394 (1983).

[79] H. Brune, K. Bromann, K. Kern, J. Jacobsen, P. Stoltze, K. Jacobsen, and J. Nørskov, Fractal and dendritic growth of surface aggregates, MRS Online Proc. Library **407**, 379 (1995).

[80] J. Yang, T. Wang, H. Wang, F. Zhu, G. Li, and D. Yan, Ultrathin-film growth of para-sexiphenyl (II): Formation of large-size domain and continuous thin film, J. Phys. Chem. B **112**, 7821 (2008).

[81] R. Batabyal, J. C. Mahato, D. Das, A. Roy, and B. N. Dev, Self-organized one-atom thick fractal nanoclusters via field-induced atomic transport, J. Appl. Phys. **114**, 64304 (2013).

[82] H. Röder, K. Bromann, H. Brune, and K. Kern, Diffusion-limited aggregation with active edge diffusion, Phys. Rev. Lett. **74**, 3217 (1995).

[83] C. Lorch, R. Banerjee, C. Frank, J. Dieterle, A. Hinderhofer, A. Gerlach, and F. Schreiber, Growth of competing crystal phases of α-sexithiophene studied by real-time in situ x-ray scattering, J. Phys. Chem. C **119**, 819 (2015).

[84] B. Servet, G. Horowitz, S. Ries, O. Lagorsse, P. Alnot, A. Yassar, F. Deloffre, P. Srivastava, and R. Hajlaoui, Polymorphism and charge transport in vacuum-evaporated sexithiophene films, Chem. Mater. **6**, 1809 (1994).

[85] B. Ranguelov, M. S. Altman, and I. Markov, Critical terrace width for step flow growth: Effect of attachment-detachment asymmetry and step permeability, Phys. Rev. B **75**, 245419 (2007).

[86] M. Campione, S. Caprioli, M. Moret, and A. Sassella, Homoepitaxial growth of α-hexathiophene, J. Phys. Chem. C **111**, 12741 (2007).

[87] F. Biscarini, R. Zamboni, P. Samorì, P. Ostoja, and C. Taliani, Growth of conjugated oligomer thin films studied by atomic-force microscopy, Phys. Rev. B **52**, 14868 (1995).

[88] D. D. C. Bradley, R. H. Friend, A. B. Holmes, R. N. Marks, F. Biscarini, T. Virgili, M. Muccini, R. Zamboni, and C. Taliani, The growth and characterization of a-sexithienyl–based light–emitting diodes, Philos. Trans. R. Soc. A **355**, 763 (1997).

[89] A. Pimpinelli, L. Tumbek, and A. Winkler, Scaling and exponent equalities in island nucleation: Novel results and application to organic films, J. Phys. Chem. Lett. **5**, 995 (2014).

[90] C. Teichert, G. Hlawacek, A. Winkler, P. Puschnig, and C. Draxl, Ehrlich-Schwoebel barriers and island nucleation in organic thin-film growth, in *Small Organic Molecules on Surfaces: Fundamentals and Applications*, edited by H. Sitter, C. Draxl, and M. Ramsey, (Springer, Berlin, 2013), pp. 79–106.

[91] A. G. Cullis, D. J. Norris, T. Walther, M. A. Migliorato, and M. Hopkinson, Epitaxial island growth and the Stranski-Krastanow transition, MRS Proc. **696**, 11 (2001).

[92] G. Richter and T. Wagner, Nucleation and growth of Pd clusters on (001) $SrTiO_3$: Determination of diffusion and adsorption energies from cluster densities, J. Appl. Phys. **98**, 94908 (2005).

[93] J. A. Venables, Nucleation and growth of thin films: Recent progress, Vacuum **33**, 701 (1983).

[94] D. Y. Zhong, M. Hirtz, W. C. Wang, R. F. Dou, L. F. Chi, and H. Fuchs, Kinetics of island formation in organic film growth, Phys. Rev. B **77**, 113404 (2008).

[95] I. Markov, Scaling behavior of the critical terrace width for step-flow growth, Phys. Rev. B **59**, 1689 (1999).

[96] F. F. Leal, S. C. Ferreira, and S. O. Ferreira, Modelling of epitaxial film growth with an Ehrlich–Schwoebel barrier dependent on the step height, J. Phys. Condens. Matter **23**, 292201 (2011).

[97] F. F. Leal, T. J. Oliveira, and S. C. Ferreira, Kinetic modelling of epitaxial film growth with up- and downward step barriers, J. Stat. Mech. (2011) P09018.

[98] W. K. Burton, N. Cabrera, and F. C. Frank, The growth of crystals and the equilibrium structure of their surfaces, Philos. Trans. R. Soc. A **243**, 299 (1997).

[99] F. Dinelli, C. Albonetti, and O. V. Kolosov, Ultrasonic force microscopy: Detection and imaging of ultra-thin molecular domains, Ultramicroscopy **111**, 267 (2011).

[100] C. Albonetti, M. Barbalinardo, S. Milita, M. Cavallini, F. Liscio, J. F. Moulin, and F. Biscarini, Selective growth of α-sexithiophene by using silicon oxides patterns, Int. J. Mol. Sci. **12**, 5719 (2011).

[101] S. Chiodini, G. D'Avino, L. Muccioli, L. Bartolini, D. Gentili, S. Toffanin, and C. Albonetti, Self-organization of complete organic monolayers via sequential post-deposition annealing, Prog. Org. Coat. **138**, 105408 (2020).

[102] M. A. Loi, E. da Como, F. Dinelli, M. Murgia, R. Zamboni, F. Biscarini, and M. Muccini, Supramolecular organization in ultra-thin films of [α]-sexithiophene on silicon dioxide, Nat. Mater. **4**, 81 (2005).

[103] S. Ohno, H. Tanaka, K. Tanaka, K. Takahashi, and M. Tanaka, Electronic structure of α-sexithiophene ultrathin films grown on, Phys. Chem. Chem. Phys. **20**, 1114 (2018).

[104] E. R. Cruz-Chu, A. Aksimentiev, and K. Schulten, Water−silica force field for simulating nanodevices, J. Phys. Chem. B **110**, 21497 (2006).

[105] Z. Shamsi and M. Foroutan, Water droplet and its contact line characteristics on hydrophobic and hydrophilic surfaces: A molecular dynamics simulation approach, J. Phys. Chem. B **129**, 2708 (2025).

[106] J. Comer, J. C. Gumbart, J. Hénin, T. Lelièvre, A. Pohorille, and C. Chipot, The adaptive biasing force method: Everything you always wanted to know but were afraid to ask, J. Phys. Chem. B **119**, 1129 (2015).

[107] M. Fendrich and J. Krug, Ehrlich-Schwoebel effect for organic molecules: Direct calculation of the step-edge barrier using empirical potentials, Phys. Rev. B **76**, 121302(R) (2007).

[108] G. Hlawacek, P. Puschnig, P. Frank, A. Winkler, C. Ambrosch-Draxl, C. Teichert, C. Ambrosch-Drax, and C. Teichert, Characterization of step-edge barriers in organic thin-film growth, Science **321**, 108 (2008).

[109] O. M. Roscioni, G. D'Avino, L. Muccioli, and C. Zannoni, Pentacene crystal growth on silica and layer-dependent step-edge barrier from atomistic simulations, J. Phys. Chem. Lett. **9**, 6900 (2018).

[110] S. C. Li, Y. Han, J. F. Jia, Q. K. Xue, and F. Liu, Determination of the Ehrlich-Schwoebel barrier in epitaxial growth of thin films, Phys. Rev. B **74**, 195428 (2006).

[111] J. E. Goose, E. L. First, and P. Clancy, Nature of step-edge barriers for small organic molecules, Phys. Rev. B **81**, 205310 (2010).

[112] V. V. Levdanskii, Dependence of the condensation (Sticking) coefficient on the radius of small aerosol particles, J. Eng. Phys. Thermophys. **75**, 792 (2002).

[113] 3M, Hydrophilicity and Surface Energy, a Little of the Science behind the Test Strip (2018).

[114] M. Kratzer, D. Wrana, K. Szajna, F. Krok, and C. Teichert, Island shape anisotropy in organic thin film growth induced by ion-beam irradiated rippled surfaces, Phys. Chem. Chem. Phys. **16**, 26112 (2014).

[115] I. Markov, Influence of surface active species on kinetics of epitaxial nucleation and growth, Mater. Chem. Phys. **49**, 93 (1997).

[116] H. R. Philipp and E. A. Taft, An optical characterization of native oxides and thin thermal oxides on silicon, J. Appl. Phys. **53**, 5224 (1982).

[117] M. J. Kim and R. W. Carpenter, Composition and structure of native oxide on silicon by high resolution analytical electron microscopy, J. Mater. Res. **5**, 347 (1990).

[118] M. Morita and T. Ohmi, Characterization and control of native oxide on silicon, Jpn. J. Appl. Phys. **33**, 370 (1994).

[119] S. Ogawa and Y. Takakuwa, Interfacial oxidation kinetics at SiO_2/Si(001) mediated by the generation of point defects: Effect of raising O_2 pressure, AIP Adv. **8**, 75119 (2018).

[120] S. T. Pantelides and M. Ramamoorthy, Atomic dynamics during silicon oxidation and the nature of defects at the Si-SiO_2 interface, MRS Online Proc. Library **490**, 59 (1997).

[121] A. X. Chu and W. B. Fowler, Theory of oxide defects near the Si-SiO_2 interface, Phys. Rev. B **41**, 5061 (1990).

[122] Y. Ishimaru, M. Yoshiki, and T. Hatanaka, The effect of dopant concentration on the native oxide growth on silicon wafer surface, MRS Proc. **259**, 405 (1992).

[123] J. A. Van Vechten and C. D. Thurmond, Entropy of ionization and temperature variation of ionization levels of defects in semiconductors, Phys. Rev. B **14**, 3539 (1976).

[124] B. Sadigh, T. J. Lenosky, S. K. Theiss, M. - J. Caturla, T. Diaz de la Rubia, and M. A. Foad, Mechanism of boron diffusion in silicon: An *ab initio* and kinetic Monte Carlo study, Phys. Rev. Lett. **83**, 4341 (1999).

[125] S. Mirabella, D. De Salvador, E. Napolitani, E. Bruno, and F. Priolo, Mechanisms of boron diffusion in silicon and germanium, J. Appl. Phys. **113**, 31101 (2013).

[126] X. - Y. Liu, W. Windl, K. M. Beardmore, and M. P. Masquelier, First-principles study of phosphorus diffusion in silicon: Interstitial- and vacancy-mediated diffusion mechanisms, Appl. Phys. Lett. **82**, 1839 (2003).

[127] P. M. Fahey, P. B. Griffin, and J. D. Plummer, Point defects and dopant diffusion in silicon, Rev. Mod. Phys. **61**, 289 (1989).

[128] D. T. Wu, Nucleation theory, *Advances in Research and Applications*, edited by H. Ehrenreich and F. Spaepen (Academic Press, 1974), Vol. 50, Chap. 9, pp. 37–187.

[129] M. Chhikara, G. Bratina, and E. Pavlica, Role of graphene topography in the initial stages of pentacene layer growth, ACS Omega **8**, 27534 (2023).

[130] M. B. Panish and H. Temkin, *Gas Source Molecular Beam Epitaxy: Growth and Properties of Phosphorus Containing III-V Heterostructures* (Springer Science & Business Media, Berlin, New York, 2013), Vol. 26.

[131] G. Horowitz, B. Bachet, A. Yassar, P. Lang, F. Demanze, J. - L. Fave, and F. Garnier, Growth and characterization of sexithiophene single crystals, Chem. Mater. **7**, 1337 (1995).

[132] Omron, FAQ00615 of temperature controllers FAQ, https://www.ia.omron.com/support/faq/answer/53/faq00615/index.html.

[133] Stats solver, simple regression calculator, https://www.statssolver.com/calculators/linear-regression.html.

[134] J. A. Stroscio, D. T. Pierce, M. D. Stiles, A. Zangwill, and L. M. Sander, Coarsening of unstable surface features during Fe (001) homoepitaxy, Phys. Rev. Lett. **75**, 4246 (1995).

[135] B. Mandelbrot, *The Fractal Geometry of Nature* (W.H. Freeman and Co., New York, 1983).

[136] D. Avnir, O. Biham, D. Lidar, and O. Malcai, Is the geometry of nature fractal? Science **279**, 39 (1998).

[137] Y. Hattori, Y. Kimura, and M. Kitamura, Nucleation density and shape of submonolayer two-dimensional islands of diphenyl dinaphthothienothiophene in vacuum deposition, J. Phys. Chem. C **124**, 1064 (2020).

[138] N. R. Wilson, P. A. Pandey, R. Beanland, J. P. Rourke, U. Lupo, G. Rowlands, and R. A. Römer, On the structure and topography of free-standing chemically modified graphene, New J. Phys. **12**, 125010 (2010).

[139] A. Rigato, F. Rico, F. Eghiaian, M. Piel, and S. Scheuring, Atomic force microscopy mechanical mapping of micropatterned cells shows adhesion geometry-dependent mechanical response on local and global scales, ACS Nano **9**, 5846 (2015).

[140] M. Brinkmann, S. Pratontep, and C. Contal, Correlated and non-correlated growth kinetics of pentacene in the submonolayer regime, Surf. Sci. **600**, 4712 (2006).

[141] I. V. Markov, *Crystal Growth for Beginners: Fundamentals of Nucleation, Crystal Growth and Epitaxy* (World Scientific, 2016), p. 632.

[142] M. A. Groce, B. R. Conrad, W. G. Cullen, A. Pimpinelli, E. D. Williams, and T. L. Einstein, Temperature-dependent nucleation and capture-zone scaling of C_{60} on silicon oxide, Surf. Sci. **606**, 53 (2012).

[143] R. G. Della Valle, E. Venuti, A. Brillante, and A. Girlando, Are crystal polymorphs predictable? the case of sexithiophene, J. Phys. Chem. A **112**, 6715 (2008).

[144] J. C. Phillips *et al.*, Scalable molecular dynamics on CPU and GPU architectures with NAMD, J. Chem. Phys. **153**, 44130 (2020).

[145] T. Darden, D. York, and L. Pedersen, Particle mesh Ewald: An $N\cdot\log(N)$ method for Ewald sums in large systems, J. Chem. Phys. **98**, 10089 (1993).

[146] N. T. Huff, E. Demiralp, T. Çagin, and W. A. Goddard, and III, Factors affecting molecular dynamics simulated vitreous silica structures, J. Non. Cryst. Solids **253**, 133 (1999).

[147] R. T. Cygan, J. - J. Liang, and A. G. Kalinichev, Molecular models of hydroxide, oxyhydroxide, and clay phases and the development of a general force field, J. Phys. Chem. B **108**, 1255 (2004).

[148] J. Wang, R. M. Wolf, J. W. Caldwell, P. A. Kollman, and D. A. Case, Development and testing of a general amber force field, J. Comput. Chem. **25**, 1157 (2004).

[149] Y. Wu, H. L. Tepper, and G. A. Voth, Flexible simple point-charge water model with improved liquid-state properties, J. Chem. Phys. **124**, 24503 (2006).

[150] L. Martínez, R. Andrade, E. G. Birgin, and J. M. Martínez, PACKMOL: A package for building initial configurations for molecular dynamics simulations, J. Comput. Chem. **30**, 2157 (2009).

[151] T. Siegrist, R. M. Fleming, R. C. Haddon, R. A. Laudise, A. J. Lovinger, H. E. Katz, P. Bridenbaugh, and D. D. Davis, The crystal structure of the high-temperature polymorph of α–hexathienyl (α–6T/HT), J. Mater. Res. **10**, 2170 (1995).

[152] A. Pizzirusso, M. Savini, L. Muccioli, and C. Zannoni, An atomistic simulation of the liquid-crystalline phases of sexithiophene, J. Mater. Chem. **21**, 125 (2011).

[153] G. D'Avino, L. Muccioli, and C. Zannoni, From chiral islands to smectic layers: A computational journey across sexithiophene morphologies on C_{60}, Adv. Funct. Mater. **25**, 1985 (2015).

[154] D. Nečas and P. Klapetek, Gwyddion: An open-source software for SPM data analysis, Cent. Eur. J. Phys. **10**, 181 (2012).